



Structural evolution of multi-walled carbon nanotube/MnO₂ composites as supercapacitor electrodes

Qiang Li^{a,b}, Jordan M. Anderson^c, Yiqing Chen^b, Lei Zhai^{c,*}

^a School of Electronic Science and Applied Physics, Hefei University of Technology, Hefei, Anhui 230009, PR China

^b School of Materials Science and Engineering, Hefei University of Technology, Hefei, Anhui 230009, PR China

^c Nanoscience Technology Center and Department of Chemistry, University of Central Florida, 12424 Research Parkway, Suite 400, Orlando, FL 32826, USA

ARTICLE INFO

Article history:

Received 29 August 2011

Received in revised form 2 November 2011

Accepted 3 November 2011

Available online 10 November 2011

Keywords:

Multi-walled carbon nanotube

Manganese oxide

Charge/discharge cycles

Structural evolution

Supercapacitor

ABSTRACT

Multi-walled carbon nanotube (MWCNT)/MnO₂ supercapacitor electrodes containing MnO₂ nanoflakes in the MWCNT network are fabricated through the oxidation of manganese acetate with poly(4-styrenesulfonic acid) (PSS) dispersed MWCNTs. The structural evolution of the electrodes under charge/discharge (reduction/oxidation) cycles and its impact on the electrodes' electrochemical properties are evaluated. Structural evolution involves the dissolution of MnO₂ upon reduction, the diffusion of the reduced Mn species from the MWCNT network toward the electrolyte solution, and the deposition of MnO₂ on the electrode surface upon oxidation. Electrode structural changes, including the electrode dissolution and the growth of the MnO₂ crystals, are scan rate dependent and have deteriorating effect on the electrode's electrochemical properties including the specific capacitance and cyclic stability.

Published by Elsevier Ltd.

1. Introduction

Electrical energy storage systems including conventional capacitors, batteries, and electrochemical capacitors or supercapacitors will play important roles in smart grids by storing energy generated from sun and wind, or other renewable energy sources [1–4]. Among them, supercapacitors are the primary choice for applications where faster- and higher-power energy storage systems are needed due to their higher energy density than conventional capacitors, and higher power density and faster power delivery than batteries [3,4]. Manganese dioxide (MnO₂) is a promising material for electrochemical supercapacitors because of its high theoretical specific capacitance (1370 F/g), fast charge–discharge process, low cost, and environmentally benign nature [5]. Energy extracted from a MnO₂ electrode strongly depends on the MnO₂ crystal morphological structure as well as the quality of the MnO₂/current collector and MnO₂/electrolyte interfaces. To improve the energy storage efficiency of MnO₂ electrodes, various MnO₂ nanostructures have been synthesized by different methods but demonstrate much lower specific capacitance than the theoretical specific capacitance [6–19]. However, composite electrodes containing MnO₂ and carbon based materials have been synthesized and demonstrate improved electrochemical performance [20–40]. Nam et al.

have recently shown that electrodeposited MnO₂ on carbon nanotubes (CNTs) displays improved electrode performance and rate capability in comparison to the electrodeposited MnO₂ film [33]. The specific capacitance of CNT/MnO₂ electrodes based on the mass of MnO₂ is ~471 F/g and the MnO₂ utilization in the CNT/MnO₂ electrode (43%) is much higher than that of 12% in electrodeposited MnO₂ films. Ternary composite structures containing dispersed multi-walled carbon nanotubes (MWCNTs), conductive polymers and MnO₂ have demonstrated a synergistic effect to enhance the electrochemical utilization of MnO₂ [41–46]. The specific capacitance of MnO₂ in these composite electrodes was estimated to be as high as 781 F/g [43]. These results demonstrate the promising potential applications of CNT/MnO₂ composites as efficient supercapacitor electrodes.

While much attention has been paid to improve the specific capacitance of active materials for supercapacitors, the structural evolution of the composite electrodes and its subsequent effect on the electrode performance during the long charge–discharge cycles should not be ignored. It has been seen that MnO₂ thin film electrodes undergo structural change in the charge/discharge (or redox) cycles, and such change results in the fading of their electrochemical performance up to 50% of the original capacitance [47–53]. The MnO₂ pseudocapacitive behavior is attributed to a Mn⁴⁺/Mn³⁺ redox system involving a single-electron transfer [5]. In aqueous electrolytes, the general charge/discharge mechanism in MnO₂-based supercapacitors can be described by: MnO₂ + M⁺ + e⁻ → MnOOM where M represents hydrated protons

* Corresponding author. Tel.: +1 407 882 2847; fax: +1 407 882 2819.
E-mail address: lzhai@mail.ucf.edu (L. Zhai).

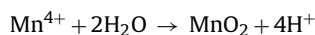
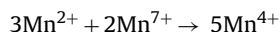
(H_3O^+) and/or alkali cations such as K^+ , Na^+ , and Li^+ . The reaction mechanism suggests a reduction/oxidation of the MnO_2 electrode accompanied by a cation adsorption/desorption at the material surface and/or insertion/extraction into the material bulk. It has been reported that MnO_2 , with crystal structures that allow for the insertion/extraction process, demonstrates high capacitance. The electrochemical performance of MnO_2 in energy storage depends on its structural parameters such as polymorphs, morphology, particle size, and bulk density [54]. Therefore, the structural change of MnO_2 is believed to cause the capacitance fading. The capacitance fading studies on electrodeposited MnO_2 suggest that the irreversible reduction of MnO_2 to Mn^{+3} species such as Mn_2O_3 and MnOOH on the electrode causes the mechanical failure or the dissolution of the electrodes [48,52]. Nanosize MnO_2 particles and large MnO_2 /current collector and MnO_2 /electrolyte interfacial area in CNT/ MnO_2 composites are expected to undergo different structural evolution from previously reported systems. Since the MnO_2 electrode morphological change is generally believed to follow an irreversible dissolution of MnO_2 at the electrode/electrolyte interface, [52] we hypothesize that the evolution of the MnO_2 crystal in the MWCNT/ MnO_2 composite follows the dissolution of MnO_2 upon reduction, the diffusion of the reduced manganese ions from CNT network toward electrolyte solution, and the deposition of MnO_2 upon oxidation.

In this paper, we report a systematic investigation of the structural evolution of MWCNT/ MnO_2 supercapacitor electrodes during the charge/discharge (or redox) cycles and the effect of such changes on the electrodes' electrochemical performance. It was found that the structural evolution of the MWCNT/ MnO_2 electrodes follows our hypothesis. The dependence of the electrode structure on the scan rate and the effect of the electrode structural change on the electrochemical properties are discussed.

2. Experimental

2.1. Synthesis of MWCNT/ MnO_2 composites

MWCNTs were purchased from Nanolab (Newton, MA) with a diameter of 10–20 nm and length about 5–20 μm . Poly(4-styrenesulfonic acid) (PSS), $\text{Mn}(\text{CH}_3\text{COO})_2 \cdot 4\text{H}_2\text{O}$ and KMnO_4 were purchased from Sigma–Aldrich (St. Louis, MO) and used as received. All aqueous solutions were prepared with triply distilled water with 18 M Ω /cm resistivity (Barnstead B–Pure). 20 mg MWCNTs and 0.4 mL 18 wt% PSS were added to 20 mL DI water followed by sonication to disperse MWCNTs. 84.5 mg $\text{Mn}(\text{CH}_3\text{COO})_2 \cdot 4\text{H}_2\text{O}$ were dissolved in 30 mL DI water, and then were stirred with the PSS dispersed MWCNTs overnight. 37 mg KMnO_4 dissolved in 50 mL DI water was added dropwise into the above solution to synthesize MWCNT/ MnO_2 composite by following the reaction.



The fabricated composite was centrifuged and washed with DI water through 3 sonication/centrifugation cycles. The resulted composite dispersion was deposited on a TEM grid and examined by TEM.

2.2. Electrode fabrication and characterization

The as-synthesized composite was mixed with Nafion (5 wt% in water) as a binder in DI water by sonication and sprayed onto the surface (1 cm \times 1 cm for each surface) of six graphite plates to build supercapacitor electrodes. All electrodes were dried in a vacuum oven for 12 h at 80 $^\circ\text{C}$. Masses of the active materials (1.8 ± 0.05 mg

on each graphite plate) were calculated by weighing the graphite plates before and after spraying/drying. In order to monitor mass changes at the surface of the modified electrodes during electrochemical measurements, Electrochemical Quartz Microbalance (EQCM) experiments were carried out on polished EQCM crystals modified with the as-synthesized composite. All EQCM crystals were obtained from Maxtek Inc. coated with a 100 Å Ti adhesion layer, followed by 1000 Å Pt. EQCM experiments were performed on a Maxtek RQCM system combined with a CHI 660B electrochemical workstation which was also used to test the electrochemical performance of the electrodes. Electrochemical measurement were performed at room temperature in a three-electrode electrochemical system containing a MWCNT/ MnO_2 composite coated graphite plate as working electrode, a platinum wire as the counter electrode, and an Ag/AgCl reference electrode. An aqueous solution of 0.5 M Na_2SO_4 was used as the electrolyte which was purged with N_2 for 10 min before electrochemical measurements were made. In order to test the impact of charge/discharge process at different scan rates on the structure and electrochemical performance of MWCNT/ MnO_2 electrodes, the electrodes were scanned 500 life-cycles (cyclic voltammetry cycles) at 20, 60, 100, 300 and 500 mV/s, and are noted as MCM20, MCM60, MCM100, MCM300 and MCM500 in the paper, respectively. The pristine as-fabricated electrode was used as a controlled sample and is noted as MCM0. The nanostructures of the samples were examined using high resolution transmission electron microscopy (HRTEM) equipped with energy dispersive X-ray spectroscopy (EDS). The composite materials were scratched off the electrode surfaces, dispersed in water, and deposited on a TEM grid for TEM examination. The surface and cross-section morphologies of the prepared electrodes before and after charge–discharge cycles were examined using field-emission scanning electron microscopy (FESEM). The chemical composition of these electrodes was analyzed by X-ray photoelectron spectroscopy (XPS).

3. Results and discussion

3.1. Characterization of material structure

The five electrodes noted as MCM20, MCM60, MCM100, MCM300 and MCM500, respectively, were used to investigate the structural change of MWCNT/ MnO_2 supercapacitor electrodes during the charge/discharge process at different scan rates. The pristine as-fabricated electrode was used as a controlled sample and is noted as MCM0. The electrode structure was investigated by studying the surface and the cross-section morphology of the electrodes using SEM, the nanostructure of the active materials using TEM, and the chemical composition of the electrode surfaces using XPS.

Fig. 1a and b shows the surface and cross section of as-synthesized MWCNT/ MnO_2 composites sprayed on a graphite substrate (MCM0). The MCM0 electrode composite has a thickness about 5.8 μm with a smooth surface morphology. The SEM images clearly show that MnO_2 nanoflakes uniformly embed in the MWCNTs network as the electrochemical storage materials while the MWCNT network works as the support of MnO_2 nanoflakes and an effective conductor of charges. In contrast, Fig. 1c–h demonstrate dramatic changes of the electrode structures after 500 CV cycles, and the structural change varies with different scan rates. Generally, it appears that MnO_2 embedded in the MWCNT network migrates from the network and deposits as cactus-like MnO_2 rods decorated with MnO_2 nanoflakes on the electrode surface. The SEM images of the surface and the cross-section of MCM20, MCM100 and MCM500 demonstrate that different structures form when the electrodes undergo 500 CV cycles at different scan rates. The MCM20 surface has MnO_2 rods with an average length around 3 μm

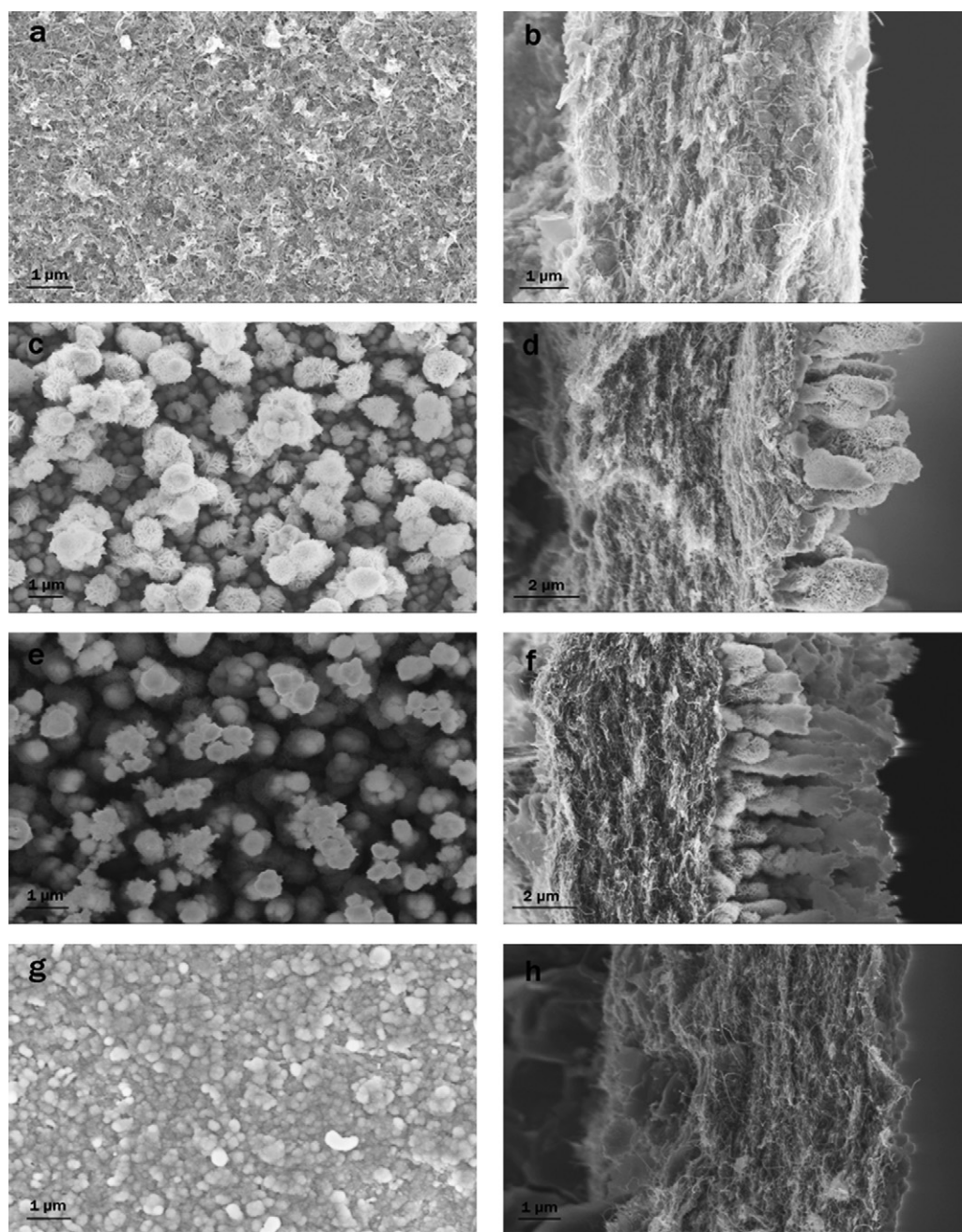


Fig. 1. Surface and cross-section morphologies of MCM0, MCM20, MCM100 and MCM500: (a) and (b) MCM0, (c) and (d) MCM20, (e) and (f) MCM100 and (g) and (h) MCM500.

and diameter about $1.5 \mu\text{m}$ (Fig. 1d) while MCM100 surface has denser MnO_2 rods with average length about $4.5 \mu\text{m}$ and diameter about $1 \mu\text{m}$ (Fig. 1f). It is interesting to observe a $0.5 \mu\text{m}$ thick film composed of sub-micron MnO_2 particles on the surface of MCM500 (Fig. 1h), indicating that a small amount of MnO_2 is deposited on the surface. The SEM images of the surface and cross-section of MCM60 and MCM300 in Fig. A.1 shows that MCM60 has an intermediate structure between MCM20 and MCM100, and MCM300 has a similar structure to MCM500, indicating a scan rate dependent structural evolution. The SEM studies of the electrodes demonstrate the pristine electrode that underwent 500 CV cycles at the scan rate of 100 mV/s (MCM100) has the most obvious structural change. The X-ray linescan spectra of Mn element also show that MnO_2 “migrates” from the MWCNTs network and “deposits” on the surface where the Mn concentration varies from the electrode surface to the MWCNT network depending on the scan rate (Fig. A.2).

The nanostructure of the as-synthesized MWCNT/ MnO_2 composite was examined using TEM. Fig. 2a shows that MnO_2 nanoflakes with a length about 50 nm and a thickness about 10 nm randomly attach on MWCNT surfaces. The energy dispersive X-ray spectroscopy (EDS) spectrum of the composites (inset in Fig. 2a) shows that the nanoflakes are composed of manganese and oxygen. The sulfur peak in the EDS spectrum is assigned to the sulfur from the PSS used to disperse MWCNTs. The carbon peak is attributed to the carbon in the MWCNT and PSS while the copper peak is generated by the copper TEM grid. The high resolution TEM image of the nanoflake (Fig. 2b) shows that the MnO_2 nanoflakes contain a variety of small MnO_2 nanoparticles about 10 nm in size. These MnO_2 nanoparticles with different crystal lattice orientations overlap on each other, causing different shapes of Moiré fringes in the high resolution TEM images.

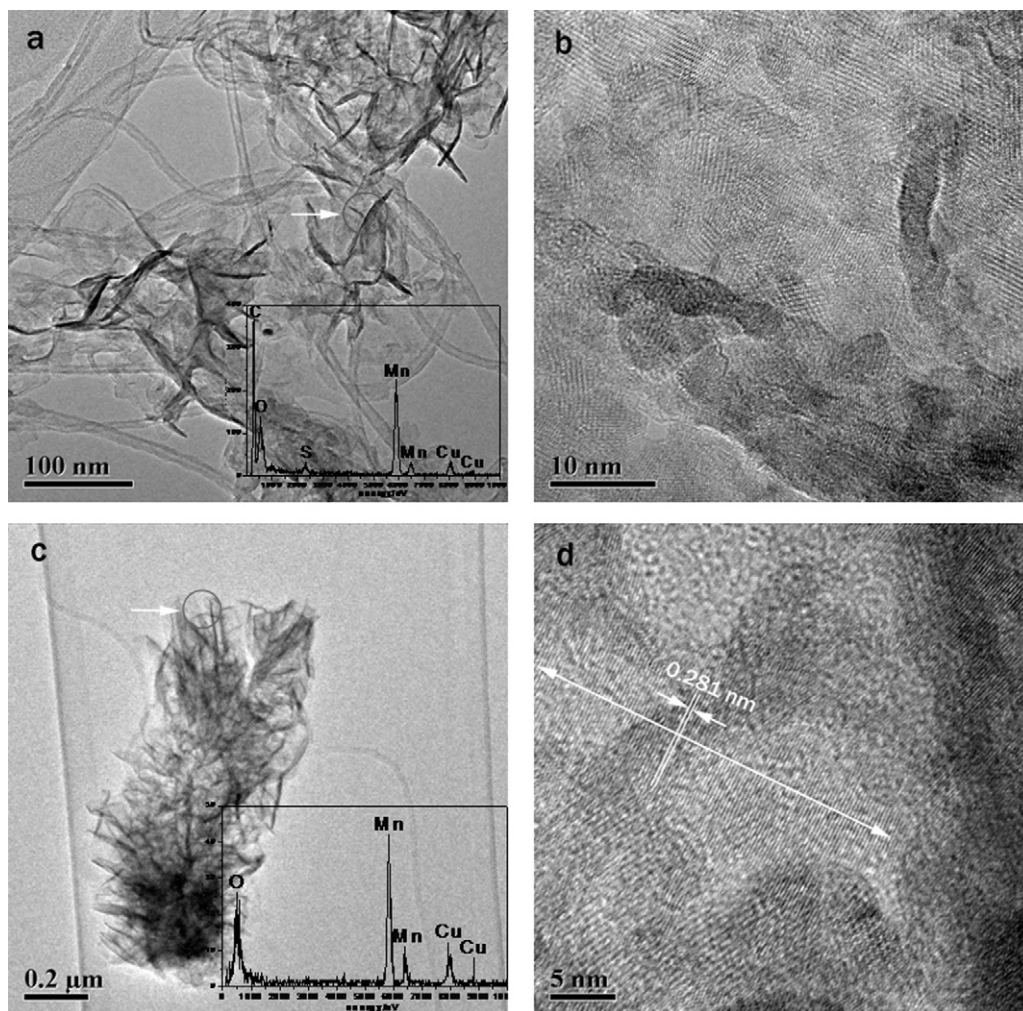


Fig. 2. TEM images of pristine MWCNT/MnO₂ and MnO₂ grown on MCM100. (a) Low magnification image of MWCNT/MnO₂, the inset is the EDS spectra of the selected area, (b) high magnification image of the selected area in (a), (c) low magnification image of MnO₂ grown on MCM100, the inset is the EDS spectra of the selected area and (d) high magnification image of the selected area in (c).

To examine the nanostructure evolution of the active materials during the charge/discharge cycles, the composite materials were collected from the MCM100 electrode (the electrode with most obvious structural change according to SEM studies) surface and examined by TEM. The microstructure of MnO₂ rods grown on the surface of MCM100 is shown in Fig. 2c. The MnO₂ rods are composed of a variety of thin MnO₂ nanoflakes. The size of these MnO₂ nanoflakes is about 0.2 μm, and an EDS spectrum of the selected nanoflake (indicated by the arrow in Fig. 2c) shows the existence of O and Mn atoms. A high resolution image of the selected nanoflake (Fig. 2d) shows that the size of one MnO₂ crystal is more than 30 nm which is larger than that of the as-synthesized MnO₂ nanoparticles in Fig. 2b. The distance between neighboring lattice fringes is 0.281 nm, as shown in Fig. 2d. The data suggests that smaller crystals, formed from fast chemical oxidation, are dissolved and re-deposited during slow oxidation processes and form larger crystals.

The electrode surfaces were investigated by XPS to determine the chemical composition before and after CV cycles. The Mn 2p spectra of all electrodes show negligible shifts of Mn 2p_{3/2} or Mn 2p_{1/2} peaks, suggesting that all electrode surfaces have a similar MnO₂ composition (Fig. 3a). The binding energies of 642.0 eV for Mn 2p_{3/2} and 653.7 eV for Mn 2p_{1/2}, with energy separation of 11.7 eV, are in agreement with Mn 2p_{3/2} and Mn 2p_{1/2} data reported previously for MnO₂ [5]. It is also found that the absolute intensities (from baseline to peak top) of Mn 2p_{3/2} and Mn 2p_{1/2} peaks in the

samples follow the order MCM100 > MCM20 > MCM500 > MCM0, and are consistent with the change tendency of Na 1s peaks in Fig. 3b. The trend in Mn and Na concentration is in good agreement with the surface morphology of the different electrodes. In Fig. 1, the SEM images of the electrodes show that MCM100 has the most MnO₂ deposited on the surface, followed by MCM20 and MCM500. With more MnO₂ on the surface, more Na ions are coordinated with the reduced Mn species, leading to higher absolute intensity of Mn 2p and Na 1s.

The SEM, TEM and XPS studies on the composite electrodes suggest that MnO₂ diffuses from MWCNT networks and deposits on the electrode's surface during the charge/discharge cycles. Comparison among the structures of MCM20, MCM60 and MCM100 indicates that the dimension of MnO₂ rods on MCM100 surface are denser, longer and thinner than those on MCM20 and MCM60 surfaces, indicating that a higher scan rate would generate more MnO₂ on the electrode surface. However, the SEM images of MCM300 and MCM500 show much less MnO₂ on the electrode surfaces compared with those of MCM20, MCM60, and MCM100, suggesting a more complicated structural evolution mechanism.

3.2. Investigation of structural evolution using EQCM

In order to better understand the structural evolution of MWCNT/MnO₂ composite electrodes upon oxidation/reduction,

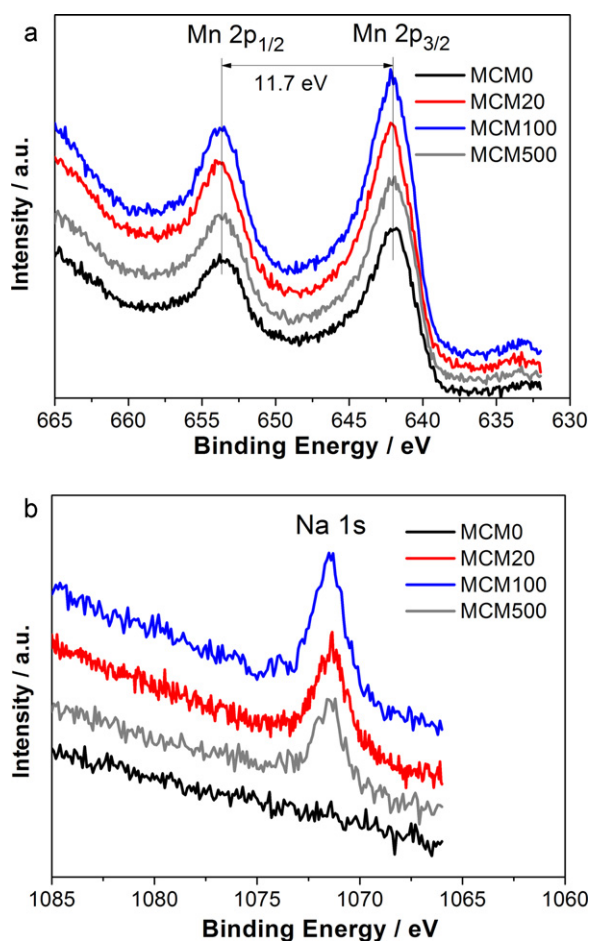


Fig. 3. XPS spectra of MCM0, MCM20, MCM100, and MCM500: (a) Mn 2p region and (b) Na 1s region.

chronoamperometry combined with EQCM was performed. An EQCM crystal was coated with MWCNT/MnO₂ composite material and then alternating voltages of 0.8 V and –0.2 V (vs. Ag/AgCl) were applied for 30 s in 0.5 M Na₂SO₄ electrolyte solution. During the chronoamperometric steps, the resonating frequency of the crystal was monitored using EQCM and converted into change in mass using the Sauerbrey equation. Results are shown in Fig. 4

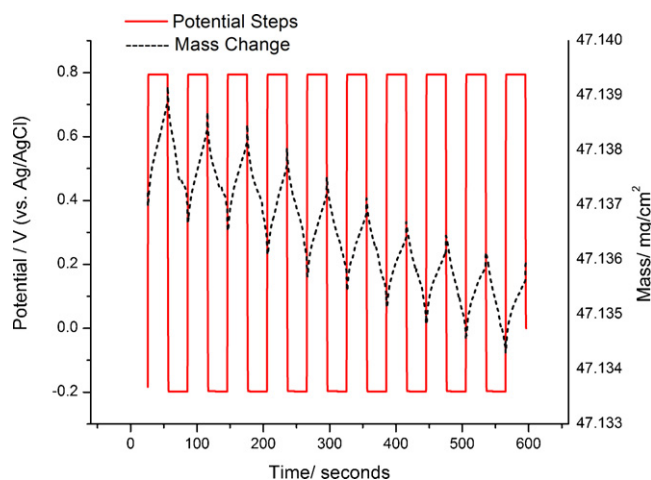


Fig. 4. Repeated 30 s chronoamperometric steps of 0.8 V and –0.2 V vs. an Ag/AgCl reference electrode. Also shown is the mass of the electrode in response to the alternating oxidation/reduction voltages.

Table 1

EQCM data showing the total and %mass loss after completion of 500 CV cycles at the given scan rates.

Electrode	Scan rate (mV/s)	Total mass loss ($\mu\text{g}/\text{cm}^2$)	% Mass loss
MCM20	20	46.027	~0.1
MCM60	60	30.578	~0.07
MCM100	100	22.406	~0.06
MCM300	300	15.865	~0.03
MCM500	500	11.634	~0.02

As seen in Fig. 4 the mass increases upon application of an oxidation potential (0.8 V) indicating the deposition of species onto the surface of the EQCM crystal. However, when a reduction potential (–0.2 V) is applied, the mass immediately begins to drop, indicating the dissolution of species from the surface of the crystal. Within each chronoamperometric step there are subsequent increases and decreases in mass determined by the potential being applied. Fig. 4 also shows the overall mass of the electrode decreasing with time as the amount of deposited MnO₂ becomes less due to the dissolution and diffusion of reduced Mn species. These results suggest that upon oxidation, MnO₂ deposits onto the surface of the electrode, while when a reduction potential is applied, reduced manganese ions diffuse from the MWCNT network toward the electrode/electrolyte interface because of the concentration gradient.

To determine the effect of scan rate on the structural evolution of MWCNT/MnO₂ composite electrodes, five identical electrodes were fabricated on the surface of EQCM crystals and scanned 500 CV cycles (from 0.8 V to –0.2 V vs. Ag/AgCl) at different scan rates (20, 60, 100, 300, 500 mV/s). During the CV scans the total mass of the electrodes was monitored using EQCM. Table 1 shows total and % mass loss data from the EQCM experiment.

It was found that the scan rate is indirectly correlated with % mass loss. The data shows a five-fold decrease in % mass loss when the scan rate is raised from 20 mV/s to 500 mV/s which indicates that a faster scan rate limits the total mass lost from the electrode. This can be explained by longer diffusion times of reduced Mn species which occurs at slower scan rates. When the reduced Mn species is allowed more time to diffuse, less MnO₂ will be re-deposited upon oxidation, leading to an electrode with an overall lower mass. When the MWCNT/MnO₂ undergoes CV cycles at a scan rate of 20 mV/s, a certain amount of MnO₂ reduces and starts to diffuse out of the MWCNT network. After ~50 s, these reduced Mn species are oxidized into MnO₂ and deposited on the electrode. At a scan rate of 100 mV/s, the higher current density generates more reduced Mn species but the diffusion time is shortened to 10 s. Such diffusion time still allows the reduced Mn species to reach the surface and be oxidized into solid MnO₂. The scan rate, therefore, has a two-fold effect on the MnO₂ structural change. The lower scan rate gives the reduced species more time to diffuse before subsequent oxidation, but the associated lower current density generates less reduced species. In contrast, the higher scan rate allows less time for the reduced species to diffuse before subsequent oxidation, but the associated higher current density produces more reduced species. This contradictory effect can be expected to generate a scan rate which causes the most dramatic structural evolution of MnO₂. SEM and TEM images show that compared with MCM20, larger amounts of reduced Mn species lead to denser MnO₂ rods and the higher current density generates thinner rods on MCM100 surface. However, at a high scan rate (such as 500 mV/s) although a large amount of MnO₂ was generated upon reduction, it had ~2 s to diffuse before being oxidized. Therefore the EQCM data suggests that at faster scan rates most MnO₂ particles remained in the MWCNT network with sub-micron particles forming on the surface.

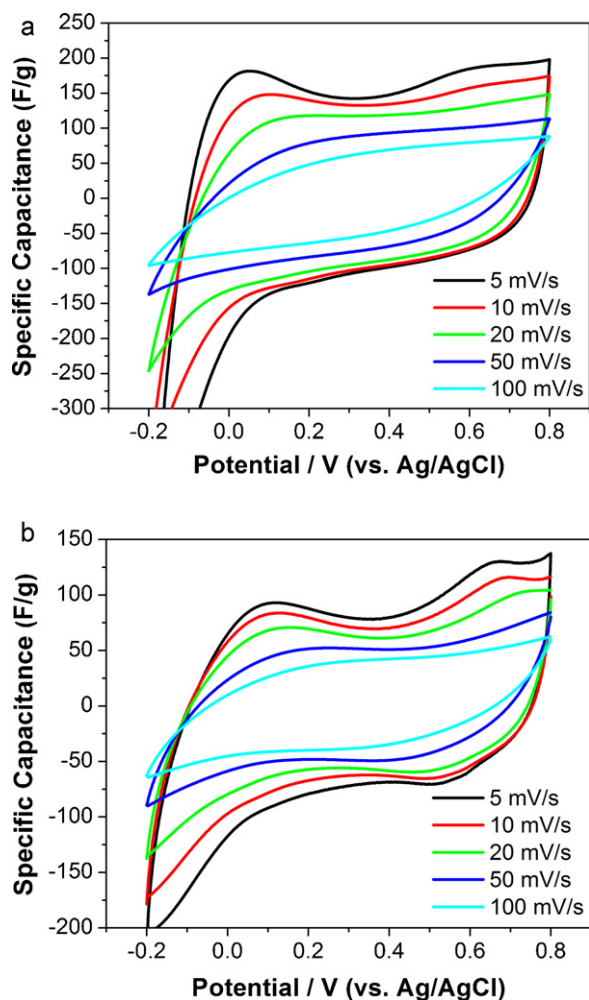


Fig. 5. (a) Cyclic voltammograms of MCM0 at various scan rates. (b) Cyclic voltammograms of MCM100 at various scan rates.

3.3. Effects of structure on electrochemical properties

The impact of the electrode structural change on the electrochemical properties was examined by cyclic voltammetry (CV) in a potential window from -0.2V to 0.8V (vs. AgCl/Ag) at various scan rates using a three-electrode system in $0.5\text{M Na}_2\text{SO}_4$ solutions. The specific capacitance (SC) was calculated from CV curves according to $C = I/mv$, where I is the current, m is the mass of reactive material, and v is the potential scan rate. The impact of the electrode structure on the electrochemical properties such as the SC was studied by comparing the CV curves of MCM0 and MCM100 (Fig. 5).

Previous SEM studies show that MCM0 has uniformly dispersed MnO_2 nanoflakes (about $10\text{ nm} \times 50\text{ nm}$, Fig. 1b) in the MWCNTs network while MCM100 has less MnO_2 nanoflakes inside MWCNT network and more MnO_2 rods (about $1\text{ }\mu\text{m} \times 4.5\text{ }\mu\text{m}$, Fig. 1f) on the surface. The TEM studies indicate that MCM100 has larger MnO_2 crystals than MCM0. Such structural distinction leads to the different electrochemical properties. The SC of each electrode decreases with the increase of the scan rate and this phenomenon can be explained by the shorter diffusion distance of Na^+/H^+ ions into the active materials at a higher scan rate that leads to lower contribution of MnO_2 . However, the SC of MCM100 is less than that of MCM0 when scanned at the same scan rate, suggesting that the MnO_2 in MCM0 is more efficiently used for the redox reaction in CV. Distinct utilization of MnO_2 is believed to be caused by the different

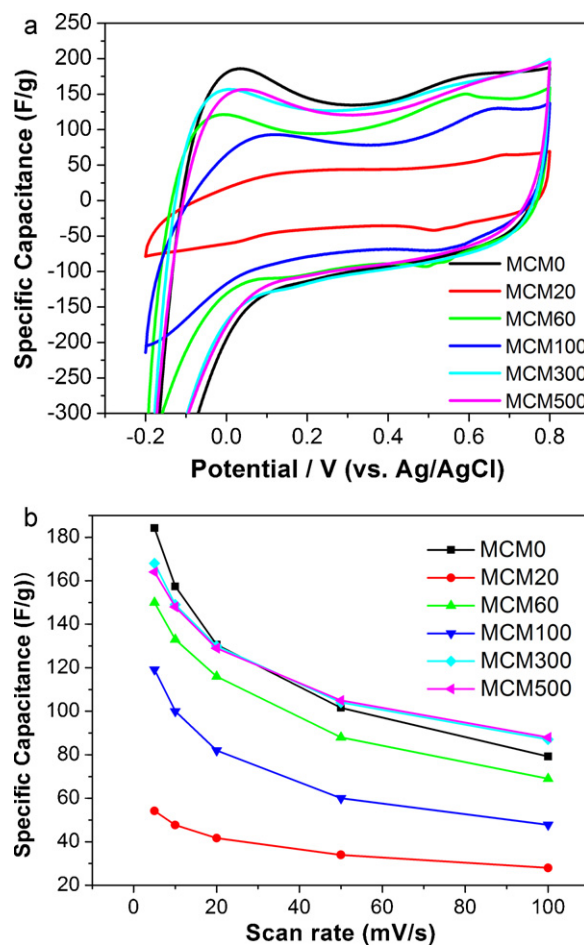


Fig. 6. (a) Cyclic voltammograms of MCM0, MCM20, MCM60, MCM100, MCM300 and MCM500 at potential scan rate of 5 mV/s . (b) Specific capacitance of MCM0, MCM20, MCM60, MCM100, MCM300 and MCM500 as a function of scan rates.

structure of MnO_2 in MCM0 and MCM100. Well dispersed MnO_2 nanoflakes in MCM0 are more accessible to Na^+/H^+ ions than the MnO_2 rods in MCM100, [50] allowing more efficient electrochemical utilization of MnO_2 in MCM0.

Fig. 6a shows the CV curves of MCM0, MCM20, MCM60, MCM100, MCM300 and MCM500 at a potential scan rate of 5 mV/s . The SC of these six electrodes follows the order of $\text{MCM0} > \text{MCM300} \approx \text{MCM500} > \text{MCM60} > \text{MCM100} > \text{MCM20}$. Such order demonstrates the impact of structural change on the SC of these six electrodes. The surface and cross-section morphologies of these electrodes (Fig. 1 and Fig. A.1) indicate that the degree of structural change follows the order of $\text{MCM0} < \text{MCM300} \approx \text{MCM500} < \text{MCM20} < \text{MCM60} < \text{MCM100}$. It is obvious that, with the exception of MCM20, electrodes with larger structural deviation from MCM0 have smaller SC. The relatively high amount of MnO_2 dissolved from MCM20 causes it to obtain the lowest SC, although MCM20 shows smaller structural change than MCM100. Fig. 6b summarizes the SCs of these electrodes as a function of scan rate from 5 mV/s to 100 mV/s and clearly indicates that the SCs heavily depend on the MnO_2 dispersion and morphologies in the electrodes which were illustrated by the SEM investigation of the electrodes (Fig. 1 and Fig. A.1).

The electrochemical impedances of MCM0, MCM20, MCM100 and MCM500 were examined over the frequency range of 10 kHz - 10 MHz at a dc bias of 0 V with a sinusoidal signal of 5 mV . Their Nyquist plots are shown in Fig. 7. The Nyquist plot of MCM0 has the curve with the largest slope at low frequency, suggesting that

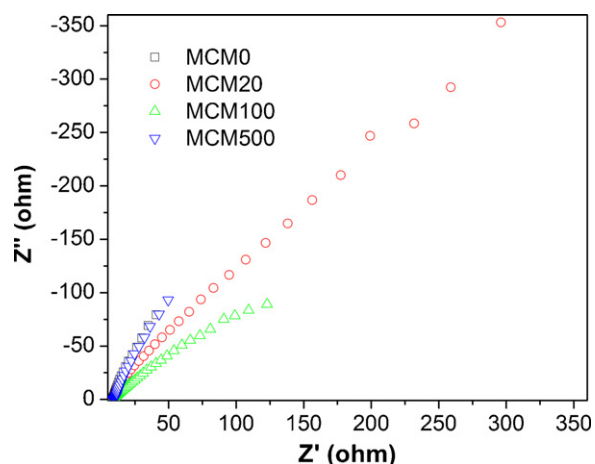


Fig. 7. Nyquist plots of MCM0, MCM20, MCM100 and MCM500 showing the changes of resistance with CV scan times.

MCM0 has the capacitance behavior closest to that of an ideal capacitor. After 500 charge/discharge cycles, MCM500 has similar capacitive performance to MCM0, but MCM20 and MCM100 show declined capacitive performances. Fig. 7 also shows that the curve length of MCM20 at low frequency is much longer than those of MCM100 and MCM500, which indicates that the ion diffusion/transport resistance of MCM20 is much higher than those of MCM100 and MCM500 [55]. Therefore, although the Nyquist slope of MCM100 is less than that of MCM20, MCM100 has better specific capacitive performance than MCM20, as shown in Fig. 6. The equivalent series resistance (ESR) at high frequency (i.e. the x -intercept of the Nyquist plots) increases slightly from 8.3Ω (MCM0) to 8.6Ω (MCM20 and MCM100) and 8.8Ω (MCM500). It is interesting to note that the interfacial charge-transfer resistances (i.e. the semicircles at the high frequency range) of MCM20 and MCM100 decrease while that of MCM500 slightly increased compared with that of MCM0. Although MCM500 has higher ESR and interfacial charge-transfer resistance than MCM20 and MCM100, the SC of MCM500 is higher than those of MCM20 and MCM100 at the same potential scan rate (Fig. 6). Therefore, the increases of the ion diffusion/transport resistances for MCM20 and MCM100 could have more negative effect on the specific capacitive behavior than the slight increase of ESR and interfacial charge-transfer resistance for MCM500. This observation is in good agreement with the reported data, which demonstrates that the SC of MnO_2 materials is mainly determined by their ionic conductivity [16].

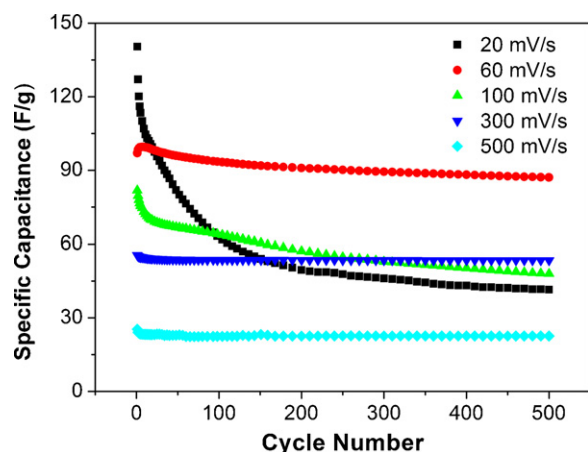


Fig. 8. Cycling stability of electrodes examined at 20, 60, 100, 300 and 500 mV/s.

The cycling stability of MWCNT/ MnO_2 electrodes (Fig. 8) indicates a capacitance decaying rate (SC retention after 500 CV cycles = the SC in the 500th cycle/the SC in the 1st cycle) in the order of MCM20 (31%) > MCM100 (60%) > MCM60 (88%) > MCM300 (93%) \approx MCM500 (92%), which demonstrates the impact of scan rate on the electrode structural evolution and the electrochemical properties. The electrode scanned at 20 mV/s starts with the highest SC followed by the electrodes scanned at 60, 100, 300 and 500 mV/s, because less time is allowed for the electrolyte ions to diffuse into the active materials when scan rate increases. However, the structural change of the electrodes has significant effect on their electrochemical stability. MCM20 undergoes significant structural change during the first 20 cycles that leads to a dramatic decrease of its SC. Although it is true that composite electrodes have better electrochemical performance at lower potential scan rates, our studies suggest that low scan rates have deteriorating effects on the electrode properties. As shown in Fig. 8, the SC of the electrodes scanned at 60, 100, and 300 mV/s exceeds the SC of the electrode scanned at 20 mV/s after 22, 98, and 160 cycles, respectively. Therefore, it is necessary to acquire a scan rate that provides the best electrochemical performance for different active materials during the long cycles in practical supercapacitor applications. In addition, the results of our studies suggest that it is possible to slow down the diffusion of reduced species by developing a charged CNT network that can form electrostatic interaction with reduced species. Such structure is currently under investigation and may allow longer electrode life time.

4. Conclusions

The structural evolution of MWCNT/ MnO_2 supercapacitor electrodes in charge/discharge cycles and the effect of the structural change on the electrochemical properties were investigated by studying the structure and electrochemical properties of identical electrodes that underwent 500 CV cycles in 0.5 M Na_2SO_4 electrolyte under different potential scan rates. Through the use of EQCM it was found that MnO_2 “migrated” from the MWCNTs network and “deposited” on the electrode surface during the charge/discharge process, which involved the dissolution of MnO_2 upon reduction, the diffusion of the reduced Mn species from the MWCNT network toward the electrolyte solution, and the deposition of MnO_2 on the electrode surface upon oxidation. Electrode structural change is influenced by two factors associated with scan rate: current density (determining the amount of materials being reduced and oxidized) and diffusion time (determining the diffusion distance of reduced species). At high scan rates, large amounts of material are reduced but the diffusion distance of the reduced species is small; however, at low scan rates the diffusion distance of the reduced species is large but the amount of reduced material is low. The combined effect leads to a scan rate (i.e. 100 mV/s) at which the most obvious structural change is observed. The effect of the electrode structural change on the electrochemical properties was studied by examining the CV curves of the electrodes. The specific capacitance of electrodes scanned at different scan rates is less than that of the pristine electrode, and the electrodes with larger structural deviation from the pristine electrode have smaller specific capacitance. Although the electrode scanned at 20 mV/s has higher specific capacitance than those scanned at a higher rate in the first 20 charge/discharge cycles, its electrochemical stability decreases dramatically due to electrode dissolution. This phenomenon suggests that a low scan rate allows high specific capacitance but may have deteriorating effects on electrode cyclic stability. Therefore, it is necessary to find the best scan rate for different active materials in order to obtain the best electrochemical performance during the long cycles in practical supercapacitor applications.

Acknowledgements

The authors are grateful to Dr. Diego J. Diaz, Dr. Qi Zhang and Kirk Scammon for their help. Qiang Li acknowledges the China Scholarship Council (No. 2009104389). The characterization support from Material Characterization Facility at the University of Central Florida and the financial support from National Science Foundation (DMR 0746499) are gratefully acknowledged.

Appendix A.

The X-ray linescan spectrum of Mn in Fig. A.2a shows that MnO_2 uniformly dispersed in the MWCNTs network of MCM0. After 500 charge/discharge cycles at different potential scan rates, MnO_2 was observed to migrate from MWCNTs network to the surface, as shown in the X-ray linescan spectra of Mn element in Fig. A.2b–f. For MCM20, MCM60 and MCM100, the MnO_2 in the MWCNTs network is very low compared to MCM0, MCM300 and MCM500.

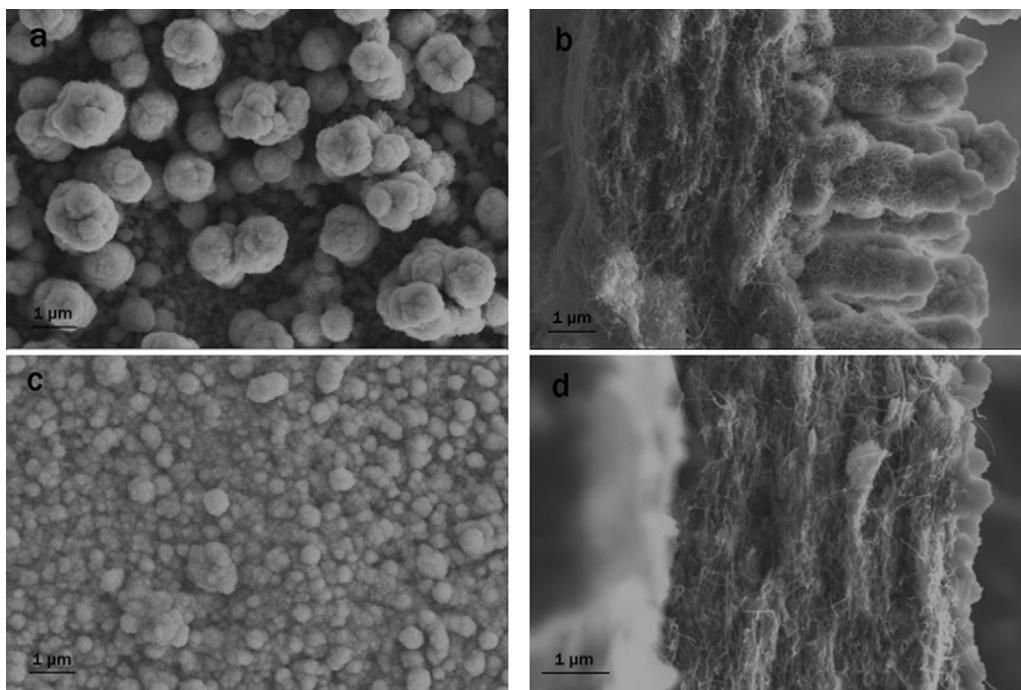


Fig. A.1. Surface and cross-section morphologies of MCM60, MCM300: (a) and (b) MCM60, (c) and (d) MCM300.

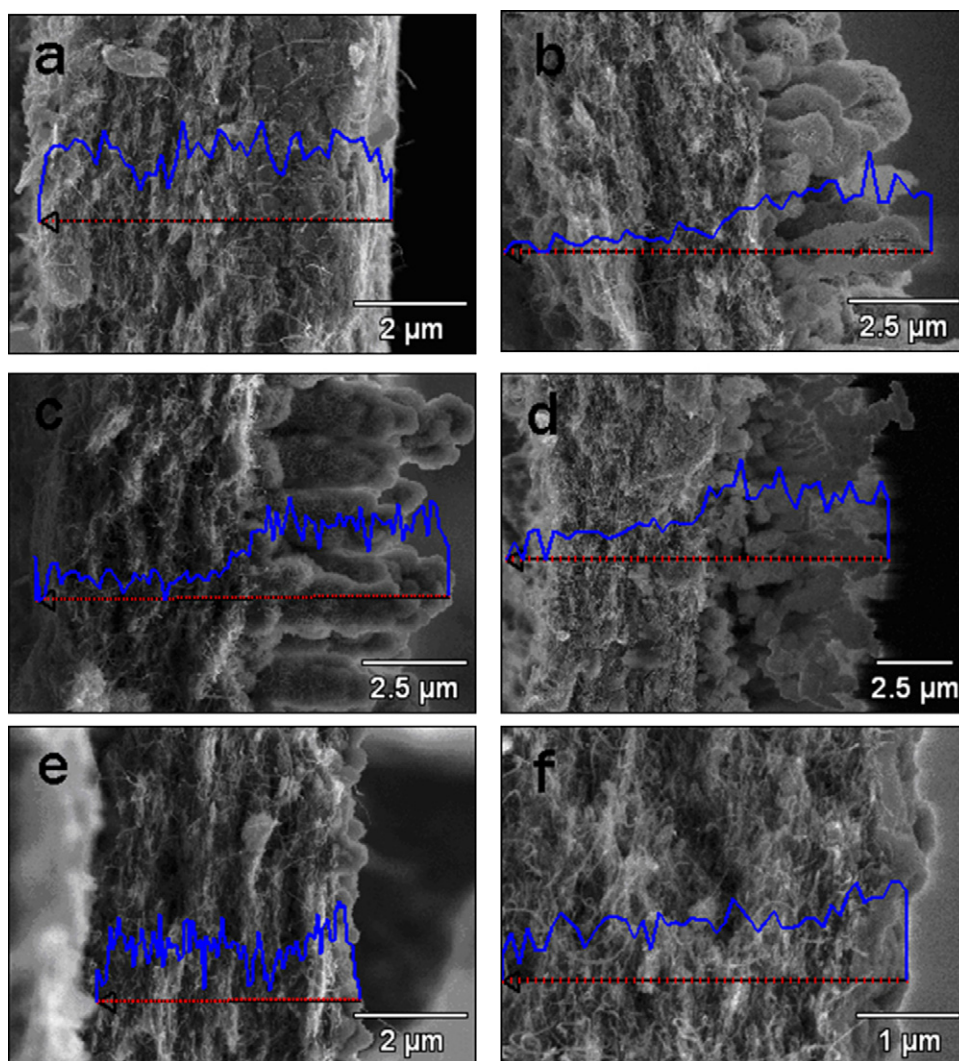


Fig. A.2. X-ray linescan spectra of Mn element in the cross-sections of: (a) MCM0, (b) MCM20, (c) MCM60, (d) MCM100, (e) MCM300, and (f) MCM500.

References

- [1] R.M. Dell, D.A.J. Rand, *J. Power Sources* 100 (2001) 2.
- [2] M. Winter, R.J. Brodd, *Chem. Rev.* 104 (2004) 4245.
- [3] P. Simon, Y. Gogotsi, *Nat. Mater.* 7 (2008) 845.
- [4] J.R. Miller, P. Simon, *Science* 321 (2008) 651.
- [5] M. Toupin, T. Brousse, D. Bélanger, *Chem. Mater.* 16 (2004) 3184.
- [6] R.N. Reddy, R.G. Reddy, *J. Power Sources* 124 (2003) 330.
- [7] T. Brousse, M. Toupin, R. Dugas, L. Athouël, O. Crosnier, D. Bélanger, *J. Electrochem. Soc.* 153 (2006) A2171.
- [8] V. Subramanian, H.W. Zhu, B.Q. Wei, *J. Power Sources* 159 (2006) 361.
- [9] M. Xu, L. Kong, W. Zhou, H. Li, *J. Phys. Chem. C* 111 (2007) 19141.
- [10] P. Yu, X. Zhang, D.L. Wang, L. Wang, Y.W. Ma, *Cryst. Growth Des.* 9 (2009) 528.
- [11] S.L. Chou, J.Z. Wang, S.Y. Chew, H.K. Liu, S.X. Dou, *Electrochem. Commun.* 10 (2008) 1724.
- [12] X.Y. Chen, X.X. Li, Y. Jiang, C.W. Shi, X.L. Li, *Solid State Commun.* 136 (2005) 94.
- [13] L. Athouël, F. Moser, R. Dugas, O. Grosnier, D. Bélanger, T. Brousse, *J. Phys. Chem. C* 112 (2008) 7270.
- [14] S. Devaraj, N. Munichandraiah, *J. Electrochem. Soc.* 154 (2007) A80.
- [15] W.F. Wei, X.W. Cui, W.X. Chen, D.G. Ivey, *J. Phys. Chem. C* 112 (2008) 15075.
- [16] O. Ghodbane, J.L. Pascal, F. Favier, *ACS Appl. Mater. Interface* 1 (2009) 1130.
- [17] Q.T. Qu, P. Zhang, B. Wang, Y.H. Chen, S. Tian, Y.P. Wu, R. Holze, *J. Phys. Chem. C* 113 (2009) 14020.
- [18] H. Xia, J.K. Feng, H.L. Wang, M.O. Lai, L. Lu, *J. Power Sources* 195 (2010) 4410.
- [19] A.J. Roberts, R.C.T. Slade, *J. Mater. Chem.* 20 (2010) 3221.
- [20] C.Y. Lee, H.M. Tsai, H.J. Chuang, S.Y. Li, P. Lin, T.Y. Tseng, *J. Electrochem. Soc.* 152 (2005) A716.
- [21] V. Subramanian, H.W. Zhu, B.Q. Wei, *Electrochem. Commun.* 8 (2006) 827.
- [22] X. Dong, W. Shen, J. Gu, L. Xiong, Y. Zhu, H. Li, J. Shi, *J. Phys. Chem. B* 110 (2006) 6015.
- [23] Y. Chen, C.G. Liu, C. Liu, G.Q. Lu, H.M. Cheng, *Mater. Res. Bull.* 42 (2007) 1935.
- [24] X. Xie, L. Gao, *Carbon* 45 (2007) 2365.
- [25] Y. Xue, Y. Chen, M.L. Zhang, Y.D. Yan, *Mater. Lett.* 62 (2008) 3884.
- [26] A.E. Fischer, K.A. Pettigrew, D.R. Rolison, R.M. Stroud, J.W. Long, *Nano Lett.* 7 (2007) 281.
- [27] J. Li, Q.M. Yang, I. Zhitomirsky, *J. Power Sources* 185 (2008) 1569.
- [28] J. Yan, Z.J. Fan, T. Wei, J. Cheng, B. Shao, K. Wang, L.P. Song, M.L. Zhang, *J. Power Sources* 194 (2009) 1202.
- [29] H.J. Zheng, F.Q. Tang, Y. Jia, L.Z. Wang, Y.C. Chen, M. Lim, L. Zhang, G.Q. Lu, *Carbon* 47 (2009) 1534.
- [30] H.J. Liu, L.H. Jin, P. He, C.X. Wang, Y.Y. Xia, *Chem. Commun.* 44 (2009) 6813.
- [31] J.M. Koa, K.M. Kimb, *Mater. Chem. Phys.* 114 (2009) 837.
- [32] R.R. Jiang, T. Huang, Y. Tang, J.L. Liu, L.G. Xue, J.H. Zhuang, A.S. Yu, *Electrochim. Acta* 54 (2009) 7173.
- [33] K.W. Nam, C.W. Lee, X.Q. Yang, B.W. Cho, W.S. Yoon, K.B. Kim, *J. Power Sources* 188 (2009) 323.
- [34] A.L.M. Reddy, M.M. Shaijumon, S.R. Gowda, P.M. Ajayan, *J. Phys. Chem. C* 114 (2010) 658.
- [35] G.R. Li, Z.P. Feng, Y.N. Ou, D.C. Wu, R.W. Fu, Y.X. Tong, *Langmuir* 26 (2010) 2209.
- [36] S. Chen, J.W. Zhu, X.D. Wu, Q.F. Han, X. Wang, *ACS Nano* 4 (2010) 2822.
- [37] H.Q. Wang, Z.S. Li, Y.G. Huang, Q.Y. Li, X.Y. Wang, *J. Mater. Chem.* 20 (2010) 3883.
- [38] M.N. Patel, X.Q. Wang, B. Wilson, D.A. Ferrer, S. Dai, K.J. Stevenson, K.P. Johnston, *J. Mater. Chem.* 20 (2010) 390.
- [39] S.W. Lee, J.Y. Kim, S. Chen, P.T. Hammond, S.H. Yang, *ACS Nano* 4 (2010) 3889.
- [40] P.C. Chen, G.Z. Shen, Y. Shi, H.T. Chen, C.W. Zhou, *ACS Nano* 4 (2010) 4403.
- [41] S.R. Sivakumar, J.M. Ko, D.Y. Kim, B.C. Kim, G.G. Wallace, *Electrochim. Acta* 52 (2007) 7377.
- [42] C.Z. Yuan, L.H. Su, B. Gao, X.G. Zhang, *Electrochim. Acta* 53 (2008) 7039.
- [43] R.K. Sharma, L. Zhai, *Electrochim. Acta* 54 (2009) 7148.

- [44] R.K. Sharma, A. Karakoti, S. Seal, L. Zhai, *J. Power Sources* 195 (2010) 1256.
- [45] Y. Hou, Y.W. Cheng, T. Hobson, J. Liu, *Nano Lett.* 10 (2010) 2727.
- [46] Q. Li, J.H. Liu, J.H. Zou, A. Chunder, Y.Q. Chen, L. Zhai, *J. Power Sources* 196 (2011) 565.
- [47] T. Brousse, P.L. Taberna, O. Crosnier, P. Guillemet, Y. Scudeller, Y.K. Zhou, F. Favier, D. Bélanger, P. Simon, *J. Power Sources* 173 (2007) 633.
- [48] Y.C. Hsieh, K.T. Lee, Y.P. Lin, N.L. Wu, S.W. Donne, *J. Power Sources* 177 (2008) 660.
- [49] S.C. Pang, M.A. Anderson, T.W. Chapman, *J. Electrochem. Soc.* 147 (2000) 444.
- [50] K.W. Nam, M.G. Kim, K.B. Kim, *J. Phys. Chem. C* 111 (2007) 749.
- [51] M.Q. Wu, G.A. Snook, G.Z. Chen, D.J. Fray, *Electrochem. Commun.* 6 (2004) 499.
- [52] W.F. Wei, X.W. Cui, W.X. Chen, D.G. Ivey, *Electrochim. Acta* 54 (2009) 2271.
- [53] W.F. Wei, X.W. Cui, W.X. Chen, D.G. Ivey, *J. Power Sources* 186 (2009) 543.
- [54] M. Toupin, T. Brousse, D. Bélanger, *Chem. Mater.* 14 (2002) 3946.
- [55] K. Zhang, L.L. Zhang, X.S. Zhao, J.S. Wu, *Chem. Mater.* 22 (2010) 1392.